A Novel Benzocyclobutene-Based Device for Studying the Dynamics of Heat Transfer During the Nucleation Process

Saeed Moghaddam, Kenneth T. Kiger, Alireza Modafe, and Reza Ghodssi, *Member, IEEE*

***Abstract*—A novel microelectromechanical device has been developed to study the details of the heat transfer mechanisms involved at the nucleation site for the nucleate boiling process. This device enables quantifying the magnitude, time period of activation, and specific areas of influence of different mechanisms of heat transfer from the surface with a resolution several times greater than previously reported. This is achieved through the use of an array of embedded temperature sensors within a carefully designed dual-layer (silicon and benzocyclobutene) wall which allows for the accurate calculation of local heat flux, circumventing difficulties encountered when using existing methods. The sensors are radially distributed around the nucleation site. Heat is supplied to the wall by a thin film heater fabricated on the outer nonwetted surface. Single bubbles are generated at the center of the array while the temperatures and the bubble images are recorded with a sampling frequency of 8 kHz. The temperature data provided the necessary thermal boundary conditions to numerically calculate the surface heat flux with an unprecedented radial resolution of 22–40 μm. Fabrication, characterization, and the ability of the developed device to elucidate the heat transfer aspects of the nucleation process are demonstrated. [2007-0016]**

***Index Terms*—Boiling, bubble, heat transfer.**

I. Introduction

BOILING HEAT transfer is generally considered one of the most efficient mechanisms of heat transfer, and as such, has been implemented in a wide variety of applications ranging from nuclear reactors to electronic cooling. Over the past 50 years, scientists have developed several competing mechanistic models to describe the boiling heat transfer process. Although the developed models are intended to predict the heat transfer coefficient at macroscales, their fundamental assumptions lie on complex microscale subprocesses that remain to be experimentally verified. Two main unresolved issues regarding these subprocesses are: 1) the mechanism of heat transfer to a growing bubble and 2) the bubble's role in enhancing surface heat transfer during the boiling process. In the following paragraphs, a brief review of existing nucleate boiling theories concerning these two issues is provided to motivate the necessity of the developed device, followed by an overview of existing contemporary efforts to develop and use microsensor arrays to study these aspects of the boiling process.

Although it is common knowledge that bubble growth on a heated wall is due to liquid evaporation at the bubble/liquid interface, the mechanism of heat transfer during this process remains unknown. The two main competing views on the mechanism of heat transfer to a bubble are typified by the models of Mikic and Rohsenow [1] and Cooper [2]. Mikic and Rohsenow [1] suggested that energy transferred into a bubble predominately comes from the superheated liquid that covers the bubble dome. In contrast, Cooper [2] suggested that evaporation of a thin liquid layer (the so-called microlayer) underneath the bubble (i.e., at the bubble/surface contact area) is the main contributing factor to the bubble growth. Numerous analytical and numerical studies (e.g., [3]–[6]) have been conducted to evaluate the accuracy of the two proposed models. Unfortunately, the lack of resolved microscale experimental data, where the phenomenon takes place, has not allowed a definitive verification of the proposed models and their fundamental assumptions.

The second unresolved issue in the boiling process is how a bubble affects the surface heat transfer in the vicinity of the nucleation site, or in a broader sense, how the individual bubbles contribute to the net energy flux from the heated surface. Different analogies/models have been developed to explain the process of heat transfer from the surface. One school of thought [7]–[12] has suggested that this heat transfer is primarily a single-phase phenomena (i.e., sensible heat transfer) that can be modeled as a convective process. The two most popular examples in this category are those of Rohsenow [11] and Mikic and Rohsenow [12]. Rohsenow [11] suggested that bubbles induce convective motions near the heated surface. He adapted a single-phase convection correlation to model the heat transfer, in which the bubble diameter and vapor superficial velocity were used as a characteristic length and velocity to define the Reynolds number. In a more detailed construct, Mikic and Rohsenow [12] postulated that heat transfer during boiling mainly takes place in a transient conduction heat transfer process. They assumed that a departing bubble pumps away the

Manuscript received January 25, 2007; revised June 20, 2007. Subject Editor O. Tabata.

S. Moghaddam is with Advanced Thermal and Environmental Concepts, Inc., College Park, MD 20740 USA, and also with the Department of Mechanical Engineering, University of Maryland, College Park, MD 20742 USA (e-mail: saeedm@umd.edu).

K. T. Kiger is with the Department of Mechanical Engineering, University of Maryland, College Park, MD 20742 USA.

A. Modafe is with the MEMS Sensors and Actuators Laboratory, Department of Electrical and Computer Engineering, University of Maryland, College Park, MD 20742 USA.

R. Ghodssi is with the MEMS Sensors and Actuators Laboratory, Department of Electrical and Computer Engineering, the Institute for Systems Research, the Fischell Department of Bioengineering, the Maryland NanoCenter, the University of Maryland Energy Research Center, and the Department of Materials Science and Engineering, University of Maryland, College Park, MD 20742 USA.

Digital Object Identifier 10.1109/JMEMS.2007.907781

1057-7157/$25.00 © 2007 IEEE

hot liquid adjacent to the surface from an area twice the bubble diameter. They approximated the heat transfer into the cooler replenishing liquid using the transient conduction solution for a semi-infinite body (the liquid). A comprehensive review of these models can also be found in [13].

Another group of models accounted for the latent heat transfer along with the sensible heat transfer to the liquid. Contribution of the latent heat to the total heat transfer from the surface has been investigated in numerous studies [14]–[17], and different models for calculating the amount of this mechanism of heat transfer from the surface have been developed. For example, Graham and Hendricks [15] suggested a combined correlation of the microlayer evaporation mechanism at the bubble growth site along with a turbulent natural convection model for the rest of the surface. Judd and Hwang [16] suggested that the microlayer evaporation could account for up to one-third of the total surface heat transfer.

In a more recent review paper, Dhir [18] suggested that by combining the contribution of transient conduction around nucleation sites, microlayer evaporation underneath the bubbles, and natural convection on inactive areas of the surface, one can determine a combined correlation that accounts for all mechanisms of heat transfer. Dhir [18] further elaborated that for this equation to be verified as a predictive tool, one needs to have several parameters: bubble diameter, bubble departure frequency, diameter of the area influenced by a single bubble, the average heat transfer coefficient for natural convection, and an average heat transfer coefficient for microlayer evaporation. For such a strategy to succeed, proper tools should be developed to accurately measure these parameters during the nucleation process.

The advent of microfabrication technology has opened an opportunity to study microscale subprocesses of boiling. Using varieties of microscale devices, different aspects of the boiling process have been studied [19]–[27]. For example, Lin *et al.* [19] studied the effect of heater width on bubble growth and departure using microheaters as small as 1 μm in width (heater width was increased from 1 to 10 μm, whereas heater length was maintained at 100 μm). Many other studies (such as [28]) attempted to determine a relation between different stages of bubble growth on a microheater array and the heat dissipation of the array. For the current work, the most relevant studies are those that have directly tried to resolve the discrepancies regarding the details of the heat transfer processes discussed earlier in this section, and as such, the studies by Demiray and Kim [25], [30] and Myers *et al.* [31] are specifically pertinent to this paper. These studies were enabled by development of a microheater array consisting of 96 rectangular platinum resistance heater elements deposited on a 0.5-mm-thick quartz substrate. The size of each heater element was $100 \times 100\ \mu\text{m}^2$, and the entire array covered a square area of 1 mm^2. The heaters were also used to measure the local surface temperature. As will be discussed later, one major challenge in these studies has been to determine an accurate value for the surface heat flux. Note that measurement of the surface temperature does not necessarily provide surface heat flux distribution. One either has all the boundary conditions for full numerical simulation of the thermal field within the wall (which then allows for the determination the surface heat flux), or else heat flux sensors should be directly fabri cated on the surface.

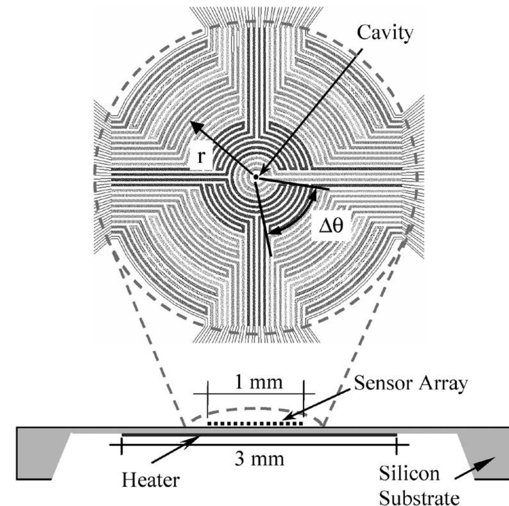

Fig. 1. Schematic of the cavity and sensor array on heated wall (see Table II for radial position of the sensors).

Through a novel design for the heated wall, fixing the nucleation site, and radial arrangement of the sensors around the nucleation site, we have been able to develop a microelectromechanical (MEM) device that allows accurate calculation of the surface heat flux with a spatial resolution of 22 to 40 μm. This paper presents the details of design and fabrication of the device and illustrates its ability to clearly elucidate the details of the heat transfer processes involved at the nucleation site.

II. Sensor Design

The device consists of a series of sensors fabricated within a composite wall surrounding an artificial cavity. The cavity generates single bubbles when heat is applied to the wall. The sensors measure the temperature of the wall/liquid surface, as well as the internal temperature of the wall at the composite boundary, enabling numerical calculation of the surface heat flux. The geometry of the sensors and the wall properties are the crucial elements of the device design. These two features are discussed in the following sections.

A. Design Criteria I: Geometry

The first layer of temperature sensors is an array of 44 radially distributed resistance temperature detectors (RTDs) on the surface of the heated wall around the cavity. The device was intended to operate with fluorinert liquids (specifically, FC-72) and hence covers a circular area of 1 mm in diameter. This is about twice the bubble diameter reported by Demiray and Kim [25], [30] for boiling of FC-72. Fig. 1 shows a schematic of the sensor array with the cavity at its center. The spatial resolution of the sensors varies between 22 and 40 μm in the radial direction, depending on location. The circular geometry of the sensor array is inspired by the nominally axisymmetric shape of a bubble and the fabrication of a fixed nucleation site, which allows for a high spatial resolution in the

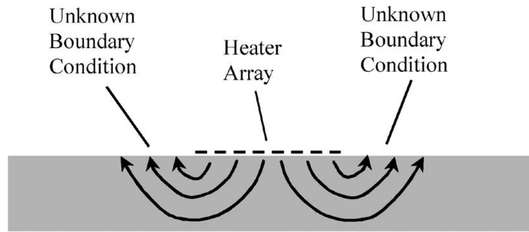

Fig. 2. Schematic cross section of the microheater array on a quartz substrate. Boundary conditions outside the array, temperature distribution within the substrate, and heat loss through the substrate are unknown.

TABLE I
THERMOPHYSICAL PROPERTIES OF BCB

Thermal conductivity [W/m.K]	0.202 [32]
Thermal capacity [J/Kg.°C]	1176+3.37*T [40]
Density [Kg/m^3]	1051 [40]

radial direction with a minimal number of sensors. Two more RTDs were fabricated within the wall. The location of these two RTDs and their function will be discussed when the wall design is described in the following sections.

B. Design Criteria II: Effect of Wall Properties

The wall thermal properties and geometry are the most critical aspects of the device design. These two parameters determine whether the surface heat flux can be accurately determined at the nucleation site. When boiling occurs within the sensor array region, it generates a heat transfer coefficient that is different from the neighboring region outside the sensor array. This leads to thermal conduction within the wall between the two regions that cannot be accounted for. As mentioned in Section I, attempts have been made in recent microscale boiling studies [29]–[31] to mitigate this issue by using a low thermal conductivity material such as quartz (a microheater array was used to both generate the heat and measure the surface temperature). However, even using quartz can result in a significant thermal conduction within the wall (see schematic in Fig. 2). As a result, some assumptions have to be made to determine the surface heat flux at the nucleation site. For example, Myers *et al.* [31] assumed that the heat transfer regime outside their 1×1 mm^2 microheater array (fabricated on a 0.5-mm-thick quartz substrate) is governed by natural convection with a heat transfer coefficient of 200 W/m$^2 \cdot$ K. Using this boundary condition for outside the microheater array area and the experimental temperature data on the microheater array, they numerically calculated the surface to fluid heat flux. Moghaddam [32] conducted an analysis of the substrate heat loss and concluded that different assumptions for thermal boundary conditions outside the array area results in significantly different values for heat flux at the array area. It was shown that the substrate heat loss can be several times greater than the surface to liquid heat flux at the array area.

In order to resolve the substrate conduction heat loss issue, we have developed a novel composite wall design that consists of a highly conducting wall, such as silicon, covered with a thin coating (in several micrometers) of a very low thermal conductivity material such as benzocyclobutene (BCB) [33].

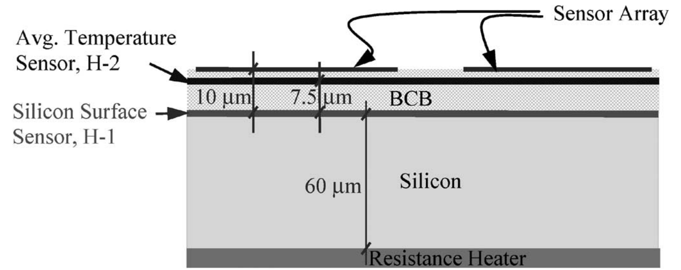

Fig. 3. Schematic cross section of the composite wall with embedded sensors. The H-1 and H-1 sensors are circular with a diameter of 1 mm. The sensor array consists of 44 sensors.

The thermal conductivity of BCB (see Table I) is one order of magnitude lower than that of quartz. In addition, BCB has favorable microfabrication properties and high-temperature stability in comparison to other low-conductivity polymers such as SU-8, polyimide, and polydimethylsiloxane. Fig. 3 shows a schematic cross section of the composite wall. The highly conductive layer of the wall maintains a nearly constant temperature beneath the insulating layer throughout the nucleation process (this was experimentally verified to be less than 0.2 °C [32]). Under these conditions, any change in the surface heat flux directly changes the temperature at the top of the BCB layer. The heat flux can then be numerically determined by modeling the heat transfer within the BCB layer, as the temperature at the bottom of the BCB layer is known (measured using temperature sensor H-1) and the boundary condition at the periphery of the sensor array region can be considered adiabatic, since the BCB layer is several micrometers thick and has a very low thermal conductivity.

It should be noted that the main reason for using a numerical model to determine the surface heat flux is that the heat transfer events underneath the bubble occur on a sufficiently short timescale that the temperature profile even in a several micrometers thick BCB layer cannot be treated as a quasi-steady case. This will be demonstrated later in the test results. If a new microfabrication material with a much lower thermal conductivity is introduced in the future such that the layer thickness (and thereby its thermal capacity) could be significantly reduced, direct reading of the heat flux could become more realistic (note that, in this case, heat flux is only a function of temperature difference between the top and bottom of the coating layer and its thermal conductivity). In such a case, the response time of the insulating layer should be one order of magnitude less than the timescale of the heat flux variations one wishes to resolve.

The thickness of the BCB layer was designed to cause a sizable temperature change at the surface during the rapid changes of the surface heat flux. Assuming a heat flux on the order of 10 W/cm^2 and using the thermal conductivity of BCB, the thickness of the BCB layer was selected to be 10 μm to achieve a temperature difference of 5 °C between the top and bottom of the BCB layer. This allows measuring a steady-state heat flux with an accuracy of 2.8% (this assumes no uncertainty in thermal conductivity and thickness of the BCB layer), given a temperature uncertainty of 0.1 °C.

As can be seen in Fig. 3, in addition to the sensor array at the top surface of the BCB layer and sensor H-1, an additional sensor (designated H-2) was incorporated to measure the total heat flux through the entire sensor array area. The integral of the heat flux values over the entire sensor array should be equal to the heat flux determined using temperature sensors H-1 and H-2.

C. Design Criteria III: Geometry of the Cavity

It is commonly known that proper thermal conditions outside a surface cavity should exist to allow bubble growth beyond the cavity mouth. A commonly used criterion for cavity activation was developed by Hsu [34]. He postulated that the temperature of the liquid surrounding the top of the bubble should exceed the temperature necessary for the bubble nucleus to remain in equilibrium. He suggested the following correlation for the radius of the active cavities:

$$r_{c,\frac{\max}{\min}} = \frac{\delta_b}{2C_1}\left[1 - \frac{\theta_s}{\theta_{\text{wall}}} \pm \sqrt{\left(1 - \frac{\theta_s}{\theta_{\text{wall}}}\right)^2 - \frac{4AC_3}{\delta_b \theta_{\text{wall}}}}\,\right] \tag{1}$$

where $\theta_s = T_{\text{sat}} - T_\infty$ (T_∞ is bulk liquid temperature), $\theta_{\text{wall}} = T_{\text{wall}} - T_{\text{sat}}$, δ_b is the thermal boundary layer thickness, and $A = 2\sigma T_{\text{sat}}/h_{\text{fg}}\rho_v$ (σ is liquid surface tension, h_{fg} is heat of vaporization, and ρ_v is vapor density). Hsu [34] suggested a set of values for constants $C_1 = 2, C_2 = 1.25$, and $C_3 = 1.6$. The boundary layer thickness $\delta_b = k_l/h$ (where k_l is the liquid thermal conductivity, and h is the convection heat transfer coefficient) was estimated to be 11 μm, using experimental results of Moghaddam *et al.* [35] for FC-72 at saturation conditions ($\theta_s = 0$) with a wall temperature of $\theta_{\text{wall}} = 25$ °C. Using (1), diameter of the active cavities was calculated to be between 0.08 and 11.9 μm. Our preliminary tests suggested that cavities with a mouth diameter of about a micrometer to a few micrometers are active in a superheat temperature range of 20 °C−40 °C, although individual cavities of a specific size were only stable over a narrower range of temperature. Best results were thus achieved with three cavities placed in close proximity, with a size ranging from approximately 0.5 to 3 μm. We also found that the cavity depth/diameter ratio affects its activation temperature and stability. A depth/diameter ratio of greater than 8–10 was found to be necessary to achieve stable nucleation. We found this to be along the line of the findings of Singh *et al.* [36]. They argued that a high depth/diameter ratio enhances the ability of a cavity to entrap gas, which is essential for its activation.

III. Microfabrication Process

The device was fabricated on a 300-μm-thick n-type $\langle 100 \rangle$ 3-in silicon wafer with a 0.3-μm-thick silicon dioxide and 0.15-μm-thick silicon nitride layers on both sides. Fig. 4 shows the microfabrication sequence. The nitride and oxide layers were patterned and etched using the reactive ion etching process over a 3.6 × 3.6 mm^2 square-shaped area on the backside of the wafer. The silicon was then etched in a 25% (by weight) potassium hydroxide (KOH) solution at 80 °C to make a 60-μm-thick membrane. Temperature sensor H-1 was fabricated on the membrane through the liftoff process and e-beam deposition of 2-nm Cr (adhesion layer) and 12-nm Ni [Ni was used because of its higher thermal coefficient of resistivity (TCR)]. A 200-nm-thick Au layer was subsequently deposited on the sensor leads. Then, a 7.5-μm-thick BCB layer was spin coated and fixed by a soft bake conducted according to the manufacturer recipe (in nitrogen atmosphere at 210 °C for 40 min) [33]. The soft or partial bake is designed to reach a 75%–82% conversion (polymerization) and is used for successive coating of the resin (i.e., double or triple coats) or multilayer structures (e.g., BCB/Metal/BCB). The H-2 sensor was then fabricated on the preceding BCB layer, with its sensing element centered and aligned to the H-1 sensor, but the leads of the two sensors rotated to the opposite side. The structure was subsequently covered with a second BCB layer (2.5 μm thick). The temperature sensor array and leads were then fabricated on the BCB layer through the liftoff process and e-beam deposition of 3-nm Cr, 12-nm Ni, and 200-nm Au. The electrical resistance of the leads was less than 2% of the total sensor resistance. The sensor array was subsequently covered with a 0.3-μm-thick BCB layer and was hard baked, according to the manufacturer recipe (in nitrogen atmosphere at 250 °C for 1 h) [33]. The BCB layer over all the bond pads was then etched. Initial trials determined that the Cr/Ni/Au wire-bond pads constructed during the sensor fabrication were not stiff enough to allow

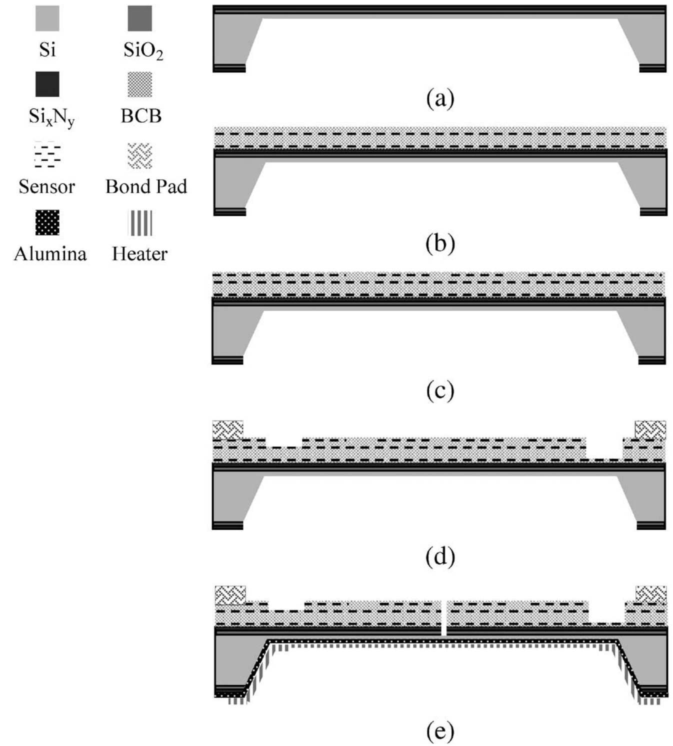

Fig. 4. Microfabrication sequence of the device. (a) Etch nitride, oxide, and silicon. (b) Fabricate H-1 sensor, spin coat, and soft bake 7.5-μm BCB, fabricate H-2 sensor, spin coat, and soft bake 2.5-μm BCB. (c) Fabricate sensor array, spin coat, and soft bake 0.3-μm BCB passivation layer. (d) Etch BCB from bond pads and fabricate Ti/Al bond pads for sensor array leads. (e) Deposit alumina on backside of membrane and fabricate heater and cavities.

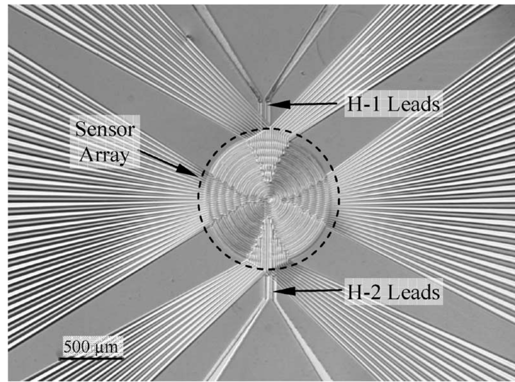

Fig. 5. Wide view of device showing sensor array leads and two pairs of leads for sensors H-1 and H-2.

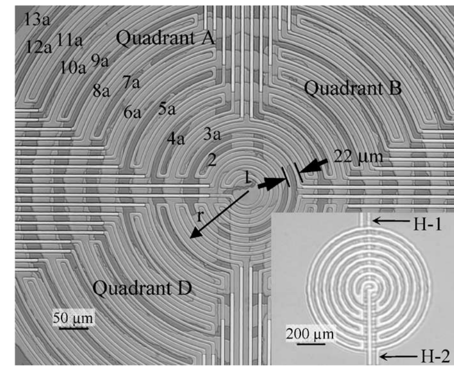

Fig. 6. Close view of device showing sensor array on top of sensors H-1 and H-2. Sensors cover circular area of 1 mm in diameter (see Table II for radial position of the sensors).

direct wire bonding. The original pads were etched and 0.5-μm Ti/1.5-μm Al bond pads were fabricated at their place. Figs. 5 and 6 show the top views of the device (Table II shows the radial position of the sensors). A 0.3-μm-thick alumina layer was then deposited on the backside of the membrane using sputtering deposition technique to provide electrical insulation. A 3×3 mm^2 chromium heater with Au leads was subsequently fabricated on the alumina layer. In the last fabrication stage, cavities were made at the center of the sensor array using focused ion beam (FIB). The main challenge in using the scanning electron microscope (SEM)/FIB machine for this process was that the sensor pattern could not be seen inside the machine, preventing the center of the array from being precisely located. This was due to the fact that the conductive sensors were covered by a nonconductive layer of BCB, rendering the sensor array invisible to the SEM. In addition, charge accumulation on the beam operation site results in beam drift. In order to overcome these difficulties, a dummy sensor array was fabricated on the final BCB layer, aligned with the actual sensor array. The dummy sensor array was fabricated by vapor deposition of a 10-nm-thick Cr layer through the liftoff process. In order to ground the dummy sensor array, the device was attached to a custom-made pin grid array (PGA) and wire bonded. The PGA pins provided the ground connection for the dummy sensor array, as the package sat on the SEM/FIB grounded stage. Three cavities were fabricated with diameters 0.7, 1.3, and 2.4 μm, as shown in Fig. 7. They are estimated to be approximately 30-μm deep. The dummy sensor array was chemically etched after fabrication of the cavities.

The TCR of the Ni sensors was measured to be around $0.001\ ^{\circ}\mathrm{C}^{-1} \pm 0.0002\ ^{\circ}\mathrm{C}^{-1}$ at $50\ ^{\circ}\mathrm{C}-90\ ^{\circ}\mathrm{C}$ temperature range. Our observed value was found to be closer to that reported for a 10-nm-thick sensor deposited on polyimide (0.0018 $^{\circ}$C^{-1} [37]) than the reported value for bulk Ni (0.0062 $^{\circ}$C^{-1}, averaged between 0 °C and 100 °C [38]).

IV. Signal Processing

Each sensor is connected to a circuit that consists of a Wheatstone bridge and an amplifier circuit. A custom-made signal conditioning board (SCB) contains these circuits along with several power supplies to power the board components and to excite the Wheatstone bridges. The change in resistance of each sensor resulting from local temperature fluctuations changes the output voltage of the circuit. The output of all circuits (output of the SCB) is directly connected to an analog-to-digital (A/D) board installed in a personal computer. Details of the board design and analysis of the Wheatstone bridge performance are available in [32].

An excitation voltage V_e of 0.400 V was applied across all the Wheatstone bridges. This resulted in a voltage across the sensors of 0.100 V for the smallest resistance (1902 Ω) and 0.178 V for the highest resistance (4616 Ω). The total energy

TABLE II
Radial Position of the Sensors

Sensor	R_{in}(μm)	R_{out}(μm)
S-1	25	66
S-2	76	100
S-3	110	134
S-4	144	185
S-5	195	236
S-6	246	270
S-7	280	304
S-8	314	338
S-9	348	372
S-10	382	406
S-11	416	440
S-12	450	474
S-13	484	491

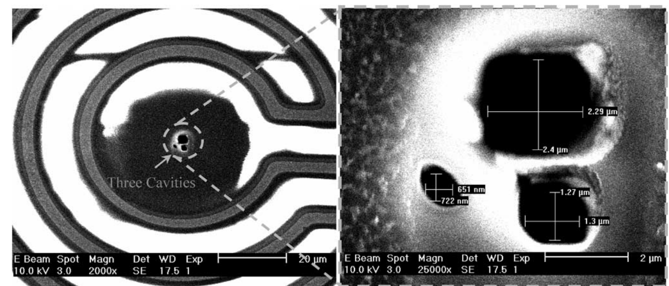

Fig. 7. SEM image of 0.7, 1.3, and 2.4 μm in diameter cavities fabricated using FIB at the center of the sensor array.

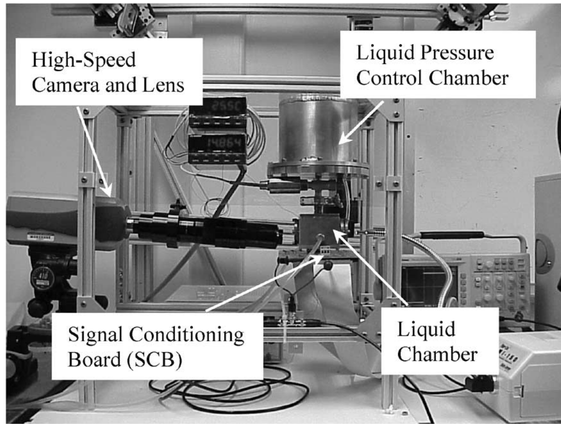

Fig. 8. Experimental setup.

dissipated in the sensor array $[\sum_{i=1}^{n}(V_i^2/R_i)]$ was 0.28 mW, which is equivalent to a heat flux of about 0.036 W/cm^2 at the sensor array area. This is two to three orders of magnitude smaller than the surface heat flux, and it indicates that self-heating from the sensor operation is negligible.

V. Experimental Apparatus

Fig. 8 shows the experimental setup. The liquid chamber is connected to a bellows enclosed within a pressure-regulated chamber in order to control the liquid pressure. A hot water line is connected to the external jacket of the liquid chamber to control the liquid temperature and to provide an isothermal condition, ensuring that liquid stratification is minimized within the chamber. Hot water is supplied to the liquid chamber external jacket by a highly stable (± 0.01 °C variation) thermal bath. A pressure transducer and four temperature sensors are installed in the liquid chamber to monitor these properties during the experiment and ensure that the test liquid is maintained at the proper conditions. A high-speed complementary metal–oxide–semiconductor camera (model Phantom 9, manufactured by Vision Solution, Inc.), which is capable of taking up to 8000 pictures/s, monitors the growth and departure process of the bubble from the surface. The camera is synchronized with the A/D board. The FC-72 test liquid used in this experiment was supplied by 3M Company.

In order to calibrate the sensors up to 95 °C, the test chamber was charged with FC-77 liquid. The boiling point of this liquid at atmospheric pressure is 97 °C. Hot water was supplied to the external jacket of the liquid chamber to adjust its temperature at different levels. The die (10×10 mm^2) temperature (i.e., temperature of the sensors) was measured with an accuracy of ± 0.1 °C using a thermocouple installed on its corner. The die was at an isothermal condition, since no heat was applied to the sensor array area.

VI. Data Reduction

Temperature of the test liquid was set at different levels by adjusting the temperature of the hot water supplied to the chamber jacket. The surface temperature was adjusted by changing the supply voltage to the thin film heater. The liquid was boiled for several hours prior to collecting data to ensure that the system is degassed. The surface temperature was increased to initiate the boiling (typically, the surface temperature was increased to about 130 °C to overcome the nucleation hysteresis, and subsequently decreased to its stable test temperature). The readings of the temperature sensors were recorded with a frequency of 8 kHz. In addition, the bubble images were captured with a rate of 8000 pictures/s. The images were processed to determine the bubble's equivalent spherical radius (estimated from the bubble outline and assuming axisymmetry) and the apparent contact line (note that the true liquid/vapor/solid contact line is obscured by the bubble). Comparison of the sensor readings within different quadrants of the array and observation of the digitized bubble images indicated that the bubble and resulting temperature field was quite axisymmetric (average temperature difference between the four quadrants was less than 0.1 °C-0.2 °C). This can be readily observed in Fig. 9, which compares the temperature data from different quadrants at several radii. In addition, comparison of the temperature results and bubble images for different bubbles suggested that the bubbling events were quite similar. These two aspects of the results have been discussed in detail in [32].

A typical test result is presented in Section VII to illustrate the device operation. The results are discussed, to a limited extent, only to show how the device reveals different aspects of the heat transfer mechanisms involved in the nucleation process. Fig. 10 shows the images of a typical bubble at a surface temperature of 86.4 °C and a liquid temperature of 56.7 °C. The first image at $t_0 = 5$ ms shows the early growth stage of a bubble formed on the surface following the departure of a preceding bubble. The bubble diameter at this stage is about 30 μm. This bubble grows and eventually departs from the surface over a period of 8 ms. Fig. 11 shows the surface temperature results corresponding to the bubbling event shown in Fig. 10.

VII. Analysis of the Experimental Results and Discussions

Comparison of the bubble images (see Fig. 10) and the temperature data (see Fig. 11) showed that the initial formation of the bubble at $t_0 = 5$ ms was associated with a sudden drop in surface temperature. The temperature drop started at the center of the array (i.e., at sensor S-1) and progressed over the subsequent sensors (i.e., sensors S-2 to S-5). Comparison of the apparent bubble contact radius with the surface temperature history showed that the temperature drop at each sensor started only after the apparent contact line passed over the sensor (see Fig. 12). This suggested that the observed temperature drop is due to surface cooling that resulted from the microlayer evaporation. The beginning of the microlayer evaporation at each sensor is marked on the temperature profiles shown in Fig. 11. As can be seen in this figure, the surface temperature started to increase shortly after the initial drop. This indicated that the microlayer was mostly evaporated and that the amount of heat supplied to the surface exceeded the cooling due to the microlayer evaporation. The increasing trend in surface

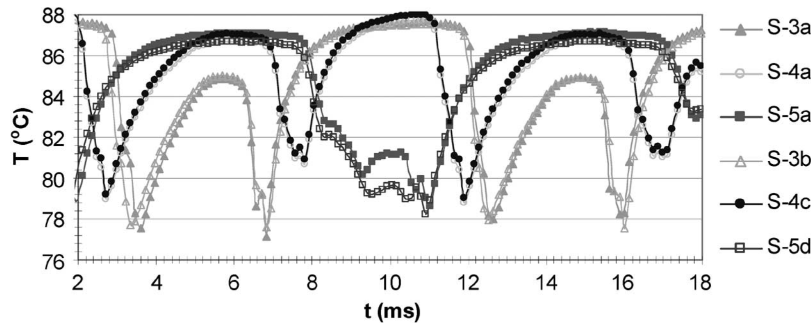

Fig. 9. Comparison of temperature data at different quadrants. Comparison of sensors S-3a with S-3b (note that sensors S-1 and S-2 are unique), and sensor S-4a with S-4c suggests excellent surface temperature symmetry. The variation in the S-5 sensors is slightly larger. A potential reason is that a small eccentricity of the bubble can cause less difference in temperature of the counterpart sensors within the contact area than the boarder sensors S-5. In this case, the contact line resides at the middle of sensors S-5 (a to d) at its maximum diameter.

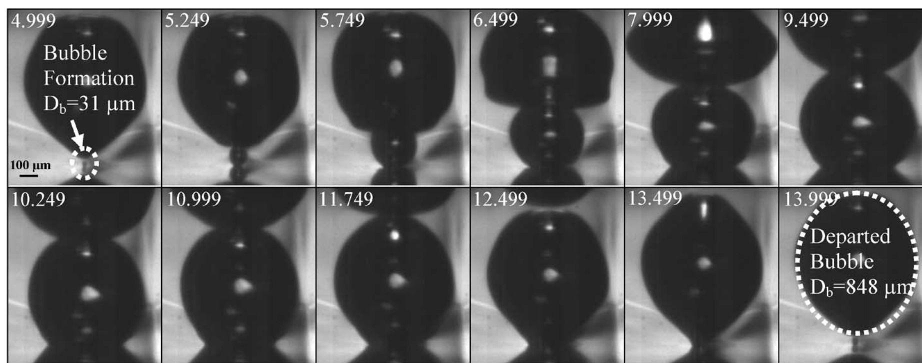

Fig. 10. Bubbling event at surface temperature of 86.4 °C (time is in milliseconds).

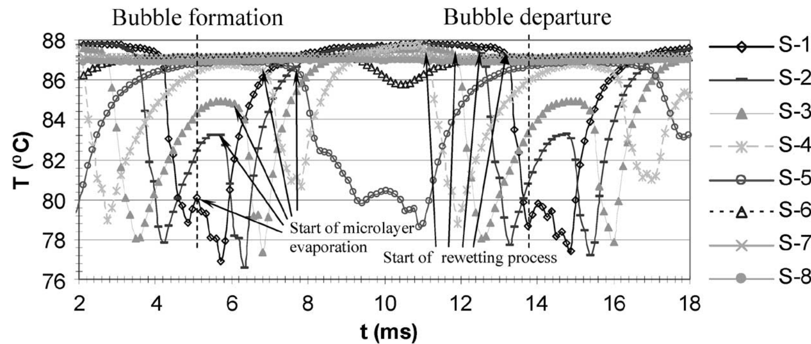

Fig. 11. Surface temperature variation during the bubbling event shown in Fig. 10.

temperature continued until the temperature of the H-1 sensor was reached.

The second phase of the surface temperature drop started after the bubble/surface contact area reached its maximum diameter and the apparent contact line started to recede. The receding liquid rewetted the dried out area. As can be seen in Fig. 11, the rewetting process began at about $t = 9.25$ ms ($t - t_0 = 4.25$ ms) when the contact line started to recede (also see Fig. 12 for comparison between the onset of temperature drop and passing time of the contact line). This resulted in a continued decrease in temperature of sensor S-5 that had already significantly decreased due to microlayer evaporation. The temperature decrease trend passed as a radially inward moving wave, corresponding to when the contact line successively passed over sensors S-4 to S-1.

As can be seen in Fig. 11, the surface temperature outside the contact area (i.e., at sensor S-6 and beyond) did not change. Note that the temperature at the bottom of the BCB layer (measured by H-1 sensor) was also constant. This suggested that heat transfer outside the contact area is steady. Further details about the nature of this mode of heat transfer will be discussed when the surface heat flux results are determined.

As mentioned in the device design section, the experimental temperature results for the top and bottom of the BCB layer provide sufficient boundary conditions to solve the thermal field

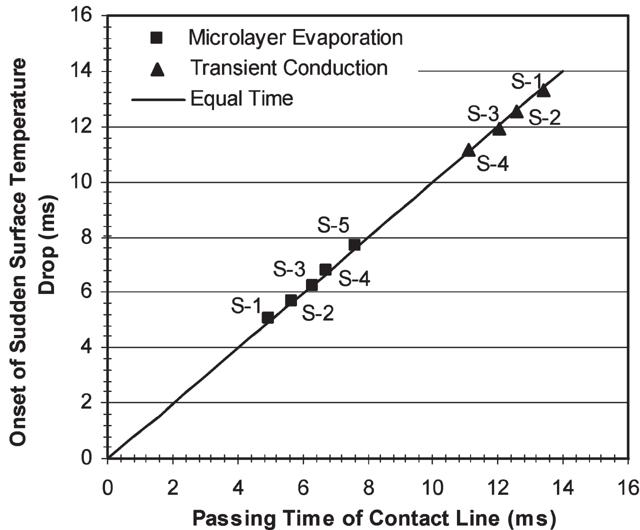

Fig. 12. Onset of sudden surface temperature drop versus passing time of the contact line. Surface temperature drop starts when the contact line passes over the sensors. Ideally, the data points should be exactly on the solid line (i.e., Equal Time). The small deviations are due to the error in measurement of the contact line location (using the bubble images) and also judgment about the exact time of surface temperature drop onset at some of the sensors.

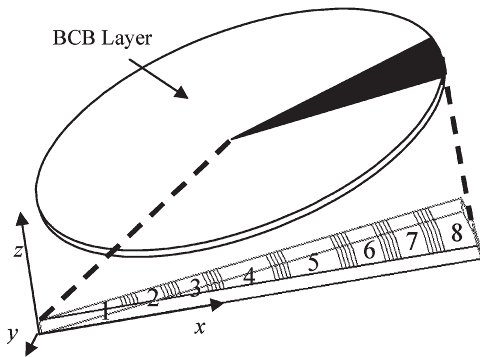

Fig. 13. Schematic of the BCB layer used for the numerical model of the BCB layer. A wedge-shaped section of the BCB layer is modeled due to temperature axisymmetry.

in the BCB layer and determine the surface heat flux. The numerical solution is discussed in Section VII-A.

A. Calculation of the Surface Heat Flux

A numerical model of the BCB layer was built using Icepak software to accurately determine the surface heat flux. Fig. 13 shows a section of the BCB layer considered for modeling. Since the temperature results were found to be axisymmetric, modeling of only a section of the BCB layer was sufficient to determine the heat flux values. This helped to reduce the mesh count and computational time. The model used a total of 144 791 nodes, with a maximum mesh size of 1, 3, and 2 μm in the x-, y-, and z-coordinate directions, respectively.

The experimental temperature values of the sensors (presented in Fig. 11) were applied to their corresponding areas on the model. The existing 10-μm-wide spaces between the sensors were divided into four sections, with their temperatures determined via linear interpolation of the nearest sensors. The other boundary conditions of the model were specified by constant temperature $T_{\text{H-1}}$ underneath the BCB layer and adiabatic conditions on its three sides. The entire model was initially set at an arbitrary temperature close to the average surface temperature. The results indicated that the initial condition effect on heat flux results diminishes in less than 2 ms (see [32] for details). The heat flux results are presented in Fig. 14.

The results reported in Fig. 14 are the most accurate representation of the actual surface heat flux. However, one might be interested to know how a heat flux calculated based on quasi-steady-state assumption ($q = k_{\text{BCB}} \Delta T_{\text{BCB}} / \Delta x$, where k_{BCB} is thermal conductivity of the BCB layer, and Δx is its thickness) compares with the numerical results. Fig. 15 shows this comparison. As can be seen in the figure, the overall trend of different events is similar for the two approaches, but the magnitude and variation rate of heat flux is significantly different due to fact that the quasi-steady assumption excludes transient term from the governing heat transfer equation. Overall, the difference is larger for faster transient events, and the peak quasi-steady heat flux values are 20%–30% smaller. However, the difference in integral of heat flux over time for different events is quite small. For instance, the total heat transfer during microlayer evaporation from all sensors calculated using the quasi-steady-state assumption is only 2.8% less than the more accurate numerically simulated value.

Uncertainties in the reported heat flux values stem from the accuracy of the temperature sensors, as well as the uncertainty in the thickness and thermal conductivity of the BCB. Temperature was measured with an accuracy of ± 0.1 °C; the thermal conductivity of the BCB layer was measured in an independent experiment to be 0.202 ± 0.008 W/m $\cdot$ K [32]; and the uncertainty in total thickness of the BCB layer was ± 0.2 μm. Comparison of the numerical heat flux values for a steady state and a transient test case, with uniform temperatures applied at the top and bottom of the model, showed a difference with theory of less than 0.4%. Therefore, contribution of the numerical error to the heat flux uncertainty was considered negligible.

Using all of these uncertainties and the root-mean-square method [39], the heat flux ($q = k_{\text{BCB}} \Delta T_{\text{BCB}} / \Delta x$) uncertainty was determined to be 4.4% and 7.4% for specific heat flux values of 30 and 3 W/cm^2, respectively. Uncertainty for all other heat flux values was determined accordingly. The higher uncertainty at low heat flux is dominated by the temperature uncertainty. This highlights the critical necessity for precise temperature measurement. The heat flux uncertainty values were used to determine the overall uncertainty in energy transfer from the surface through each mechanism (note that the energy transfer from the surface is integral of heat flux over time).

B. Analysis of the Heat Flux Results

1) Microlayer Evaporation: As can be seen in Fig. 14, initiation of the microlayer evaporation shortly after formation of the bubble (at $t_0 = 5$ ms) resulted in heat flux spikes of up to about 30 W/cm^2 over the contact area. The durations of these spikes were on the order of 1 ms and corresponded to the lifetime of the layer over the respective sensor. The areas

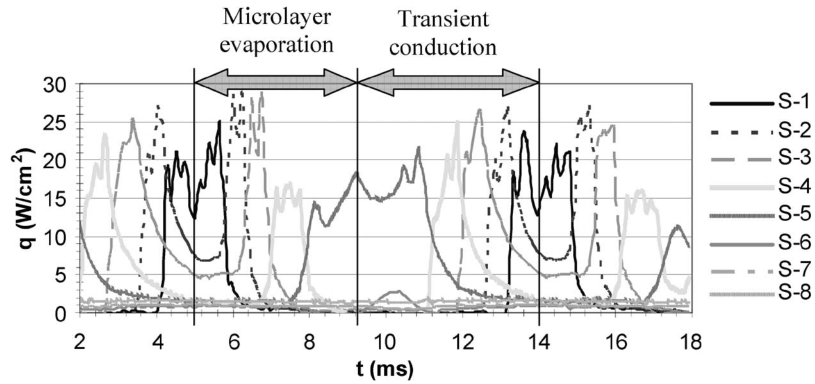

Fig. 14. Heat flux results corresponding to the temperature data in Fig. 11. Heat transfer due to microlayer evaporation and transient conduction is marked.

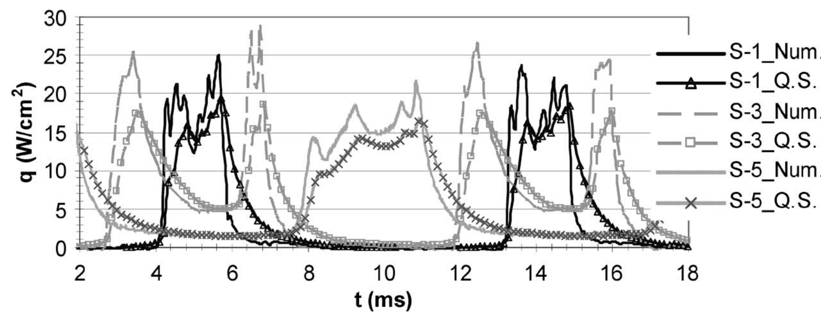

Fig. 15. Comparison between the numerically calculated heat flux (shown with Num. extension) and the heat flux calculated using quasi-steady-state assumption (shown with Q.S. extension).

under the heat flux curves show local energy transfer from the surface during the microlayer evaporation. The heat flux values were multiplied by the area of their corresponding sensors and added up together to determine the overall heat transfer from the surface due to microlayer evaporation. This was determined to be 32.2 ± 1.8 μJ at the end of the microlayer evaporation process.

Microlayer thickness and contribution to bubble growth: As mentioned in Section I, an unresolved issue in the boiling literature is the contribution of microlayer energy to the total energy transfer into the bubble. The microlayer evaporation energy can be broken into two parts: 1) direct heat transfer from the heated wall ($\int_{t_{m,i}}^{t_{m,e}} q_{s,m} A dt$) during the microlayer evaporation, where $q_{s,m}$ is the wall heat flux during the microlayer evaporation, and $t_{m,i}$ and $t_{m,e}$ are times marking the beginning and end of the microlayer evaporation, respectively, and 2) the initial sensible energy of the liquid microlayer trapped beneath the bubble ($mC\Delta T$). The sum of these two components is related to the microlayer evaporation energy through the following equation:

$$\int_{t_{m,i}}^{t_{m,e}} q_{s,m} A dt + mC\Delta T = m h_{\rm fg} \quad (2)$$

where ΔT is the difference between the initial layer-averaged temperature of the microlayer and the saturation temperature of the liquid, which is referred to as the initial equivalent superheat

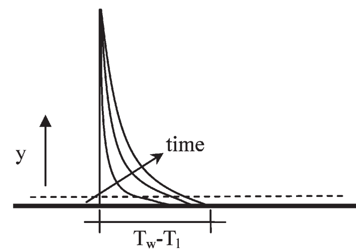

Fig. 16. Schematic of temperature profile within the liquid before the microlayer formation.

temperature. Equation (2) can be expanded to the following form:

$$\int_{t_{m,i}}^{t_{m,e}} q_{s,m} A dt + \rho_l A \delta_0 C \Delta T = \rho_l A \delta_0 h_{\rm fg}. \quad (3)$$

After canceling A and rearranging the terms, the initial microlayer thickness δ_0 can be determined as follows:

$$\delta_0 = \int_{t_{m,i}}^{t_{m,e}} q_{s,m} dt / (\rho_l h_{\rm fg} - \rho_l C \Delta T). \quad (4)$$

Before one could use (4) to calculate the initial microlayer thickness, the initial equivalent superheat temperature of the microlayer ΔT should be determined. Since the surface temperature and heat flux at the time of microlayer formation are

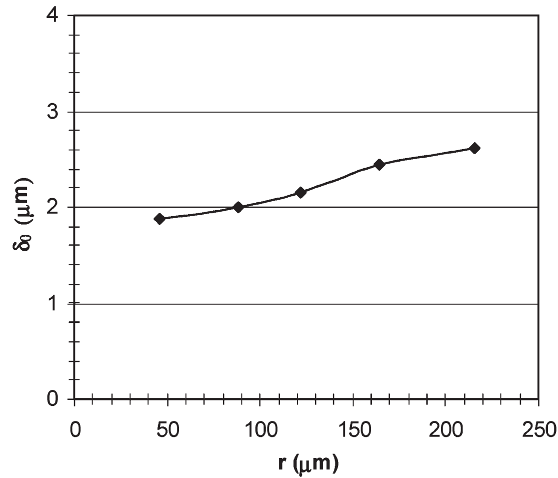

Fig. 17. Microlayer thickness versus radius from the center of the bubble at average surface temperature of 86.4 °C.

known, the initial temperature profile in the vicinity of the wall can be directly calculated. Fig. 16 shows a schematic of the liquid temperature profile during the transient conduction heat transfer process. Knowing the surface heat flux, the slope of the temperature profile at the liquid and surface interface $dT/dy = q/k_l$ can be determined. Since the microlayer is only a few micrometers thick, the temperature profile within the microlayer can be reasonably approximated as linear. Since the temperature at the bottom of the microlayer film is equal to the wall temperature, and the temperature gradient within the liquid is determined, the average temperature of the microlayer (and thereby ΔT) can be calculated. Using (4), the initial (maximum) thickness of the microlayer on each sensor was determined and presented in Fig. 17. It is important to emphasize that the microlayer profile shown in Fig. 17 does not physically exist on the surface at any time during the microlayer formation and evaporation. This is due to the fact that the microlayer rapidly evaporates as it forms over the surface, so its thickness over all the sensors is never simultaneously equal to the initial thickness. The heat flux results suggest that the microlayer fully evaporates at the smaller radii even before the apparent bubble contact diameter (and hence the microlayer) has reached its maximum extent. The thickness of the microlayer would have been equal to what is shown in Fig. 17, if it had not evaporated before it was fully formed.

The total microlayer energy can then be determined using the following expression:

$$Q_m = \rho_l A \delta_0 h_{\text{fg}}. \tag{5}$$

The total microlayer energy (latent and sensible heat) was determined to be $53.2 \pm 2.9\ \mu$J. Since the evaporation of the microlayer simultaneously removes heat from the wall while contributing to the growth of the bubble, it is useful to compare the magnitude of this mechanism to the energy required to produce the bubble. Using the final bubble diameter (848 μm), the total bubble energy was determined to be 361.9 μJ, making the microlayer contribution to the total bubble energy 14.7% for the test conditions presented in this paper.

2) Transient Conduction: The second wave of heat flux spikes initiated when the contact line started to recede at $t = 9.25$ ms. This mechanism of heat transfer to the liquid clearly has a transient nature and can be considered to be what is commonly referred to as transient conduction heat transfer. As can be seen in Fig. 14, transient conduction heat transfer peaked after microlayer evaporation and significantly declined before the bubble departure. The area of influence of this mechanism of heat transfer is limited to the bubble/surface contact area that is approximately $0.5D$ in diameter. The total transient conduction heat transfer from the surface can be determined by multiplying the cumulative heat transfer values by the area of their corresponding sensors and adding them together. The total transient conduction heat transfer was thus determined to be $54.0 \pm 3.0\ \mu$J.

3) Microconvection: As mentioned earlier, the surface temperature outside the contact area remained constant throughout the ebullition cycle. Considering that the bottom temperature of the BCB layer $T_{\text{H-1}}$ was also constant, the surface heat flux outside the contact area remained constant during the bubble formation and departure process. The value of this heat flux was determined using the following equation:

$$q = k_{\text{BCB}}(T_{\text{H-1}} - T_s)/\Delta x \tag{6}$$

where $T_{\text{H-1}}$ and T_s are the temperatures at the bottom and top of the BCB layer, respectively. Using this equation, the surface heat flux outside the contact area was determined to be 1.52 ± 0.19 W/cm^2. This is equivalent to $53.1 \pm 6.7\ \mu$J energy transfer over a surface area of 3.91×10^{-3} cm^2 (projection area of the bubble minus the contact area) during one bubbling cycle.

Although the test results suggested that the surface heat flux outside the contact area was steady (i.e., did not change during the bubble growth and departure), it was important to determine whether the bubble influenced that heat flux or whether it was simply equal to that of the natural convection. In order to investigate this important aspect, natural convection heat flux from the surface was measured at the same surface temperature that was used for the boiling test (86.4 °C). This was accomplished by taking advantage of the significant temperature hysteresis (up to about 130 °C) of the current working conditions. The natural convection heat flux was measured to be 0.84 ± 0.18 W/cm^2. This suggested that heat flux outside the contact area during the bubbling process was 1.8 times greater than the natural convection heat flux at this particular test condition. This clearly indicated that bubbling events generated an almost constant enhanced convection effect in the vicinity of the contact area, which can be identified as the microconvection mechanism qualitatively described in previous studies.

a) Comparison of the heat transfer mechanisms: As the experimental results revealed, the nucleation process triggered three mechanisms of heat transfer at the nucleation site including: 1) microlayer evaporation; 2) transient conduction; and 3) microconvection. As discussed, these mechanisms of heat transfer were active during different periods of time and within specific locations underneath and around the bubble. The contributions of these mechanisms of heat transfer from the surface within a circular area of diameter equal to that of

the bubble was 23.1% ($32.2 \pm 1.8\ \mu$J) for microlayer, 38.8% ($54.0 \pm 3.0\ \mu$J) for transient conduction, and 38.1% ($53.1 \pm 6.7\ \mu$J) for microconvection for the given conditions of the test.

It should also be noted that the total energy transfer from the circular area of diameter equal to that of the bubble (i.e., bubble-projected area) is significantly less than the bubble total energy at departure time (361.9 μJ). This is because the bubble acquires a significant amount of its energy from the liquid heated outside the bubble-projected area. This liquid approaches the bubble region during the rewetting phase/departure of an earlier bubble (this liquid later surrounds the bubble as it emerges from the cavity) and when it rises around the growing bubble as a liquid plume.

To the best of our knowledge, Figs. 11 and 14 along with the synchronized images in Fig. 10 provided the most detailed experimental results on characteristics of different heat transfer events and their relation to the bubble growth stages. This includes the sequence of the events and their time duration, area of influence, and magnitude. This device can be used to study the dynamics of heat transfer at the nucleation site as a function of wall superheat, liquid conditions, and cavity size and geometry.

VIII. Conclusion

The design and fabrication process of a novel MEM device for studying the heat transfer processes involved at the nucleation site was presented. The device has enabled resolving the thermal field with an unprecedented spatial resolution of 22–40 μm. The ability of the device was demonstrated through analyzing a typical test result. The results provided spatial localization, time period of activation, and magnitude of different mechanisms of heat transfer active at the nucleation site. The results also allowed determining contribution of the microlayer in bubble growth. This device can be used to study the heat transfer processes involved at the nucleation site under different conditions.

References

[1] B. B. Mikic and W. M. Rohsenow, "Bubble growth rates in non-uniform temperature field," *Prog. Heat Mass Transfer*, vol. 2, pp. 283–292, 1969.

[2] M. G. Cooper, "The microlayer and bubble growth in nucleate pool boiling," *Int. J. Heat Mass Transfer*, vol. 12, no. 8, pp. 915–933, Aug. 1969.

[3] R. Mei, W. Chen, and J. F. Klausner, "Vapor bubble growth in heterogeneous boiling—I. Formulation," *Int. J. Heat Mass Transfer*, vol. 38, no. 5, pp. 909–919, Mar. 1995.

[4] R. Mei, W. Chen, and J. F. Klausner, "Vapor bubble growth in heterogeneous boiling—II. Growth rate and thermal fields," *Int. J. Heat Mass Transfer*, vol. 38, no. 5, pp. 921–934, Mar. 1995.

[5] A. J. Robinson and R. L. Judd, "Bubble growth in a uniform and spatially distributed temperature field," *Int. J. Heat Mass Transfer*, vol. 44, no. 14, pp. 2699–2710, Jul. 2001.

[6] G. Son, V. K. Dhir, and N. Ramanujapu, "Dynamics and heat transfer associated with a single bubble during nucleated boiling on a horizontal surface," *J. Heat Transfer*, vol. 121, pp. 623–631, 1999.

[7] M. Jakob and W. Linke, "Boiling heat transfer," *Phys. Z.*, vol. 636, pp. 267–273, 1935.

[8] H. K. Forster and N. Zuber, "Dynamic of vapor bubbles and boiling heat transfer," *AIChE J.*, vol. 1, pp. 531–539, 1955.

[9] C. L. Tien, "Hydrodynamic model for nucleate pool boiling," *Int. J. Heat Mass Transfer*, vol. 5, no. 6, pp. 533–540, Jun. 1962.

[10] N. Zuber, "Nucleate boiling the region of isolated bubbles and the similarity with natural convection," *Int. J. Heat Mass Transfer*, vol. 6, no. 1, pp. 53–78, Jan. 1963.

[11] W. M. Rohsenow, "A method of correlating heat transfer data for surface boiling of liquids," *Trans. ASME, J. Heat Transfer*, vol. 74, pp. 969–976, 1951.

[12] B. B. Mikic and W. M. Rohsenow, "A new correlation of pool-boiling data including the effect of heating surface characteristics," *Trans. ASME, J. Heat Transfer*, vol. 91, pp. 245–250, 1969.

[13] S. Moghaddam and K. Kiger, "Pool boiling mechanism of HFE-7100," in *Proc. ASME Heat Transfer/Fluids Eng. Summer Conf.*, Charlotte, NC, Jul. 11–15, 2004.

[14] C. J. Rallis and H. H. Jawurek, "Latent heat transfer in saturated nucleate boiling," *Int. J. Heat Mass Transfer*, vol. 7, pp. 1051–1068, 1964.

[15] R. W. Graham and R. C. Hendricks, "Assessment of convection, conduction, and evaporation in nucleate boiling," NASA, Cleveland, OH, NASA TN D-3943, 1967.

[16] R. L. Judd and K. S. Hwang, "A comprehensive model for nucleate pool boiling heat transfer including microlayer evaporation," *Trans. ASME, J. Heat Transfer*, vol. 98, no. 4, pp. 623–629, 1976.

[17] R. J. Benjamin and A. R. Balakrishnan, "Nucleate pooling heat transfer of pure liquids at low to moderate heat fluxes," *Int. J. Heat Mass Transfer*, vol. 39, pp. 2495–2504, 1996.

[18] V. K. Dhir, "Boiling heat transfer," *Annu. Rev. Fluid Mech.*, vol. 30, pp. 365–401, 1998.

[19] M. T. Lin, W. J. Yang, and L. Lin, "A preliminary study of boiling on micro line heaters," in *Proc. 11th Int. Symp. Transport Phenomena*, Hsinchu, Taiwan, R.O.C., 1998, pp. 492–506.

[20] L. Lin, A. P. Pisano, and V. P. Carey, "Thermal bubble formation on polysilicon micro resistors," *Trans. ASME, J. Heat Transfer*, vol. 120, no. 3, pp. 735–742, Aug. 1998.

[21] T. Shimokubo, S. Takagi, and T. Inoue, "Boiling bubble behavior from the micro heater," in *Proc. 35th Heat Transfer Symp. Jpn.*, 1998, pp. 173–174.

[22] T. D. Rule and J. Kim, "Heat transfer behavior on small horizontal heaters during pool boiling of FC-72," *Trans. ASME, J. Heat Transfer*, vol. 121, no. 2, pp. 386–393, 1999.

[23] W. J. Yang, "Overview of boiling on microstructures: Macro bubbles from micro heaters," *Microscale Thermophys. Eng.*, vol. 4, no. 1, pp. 7–24, Jan. 2000.

[24] J. H. Tsai and L. Lin, "Transient thermal bubble formation on polysilicon micro-resistors," *Trans. ASME, J. Heat Transfer*, vol. 124, no. 2, pp. 375–382, 2002.

[25] F. Demiray and J. Kim, "Heat transfer from a single bubble nucleation site during saturated pool boiling of FC-72 using an array of 100 micron heaters," in *Proc. 8th AIAA/ASME Joint Thermophysics and Heat Transfer Conf.*, St. Louis, MO, 2002, pp. 1–12.

[26] H. C. Lee, B. D. Oh, S. W. Bae, and M. H. Kim, "Single bubble growth in saturated pool boiling on a constant wall temperature surface," *Int. J. Multiph. Flow*, vol. 29, no. 12, pp. 1857–1874, Dec. 2003.

[27] T. Chen and J. N. Chung, "An experimental study of miniature-scale pool boiling," *Trans. ASME, J. Heat Transfer*, vol. 125, no. 6, pp. 1074–1086, Dec. 2003.

[28] H. C. Lee, B. D. Oh, S. W. Bae, M. H. Kim, J. Y. Lee, and I. S. Song, "Partial nucleate boiling on the microscale heater maintaining constant wall temperature," *J. Nucl. Sci. Technol.*, vol. 40, no. 10, pp. 768–774, Oct. 2003.

[29] C. D. Henry and J. Kim, "Heater size, subcooling, and gravity effects on pool boiling heat transfer," *Int. J. Heat Mass Transfer*, vol. 25, pp. 262–273, 2004.

[30] F. Demiray and J. Kim, "Microscale heat transfer measurements during pool boiling of FC-72: Effect of subcooling," *Int. J. Heat Mass Transfer*, vol. 47, no. 14–16, pp. 3257–3268, Jul. 2004.

[31] J. G. Myers, V. K. Yerramilli, S. W. Hussey, G. F. Yee, and J. Kim, "Time and space resolved wall temperature and heat flux measurements during nucleate boiling with constant heat flux boundary conditions," *Int. J. Heat Mass Transfer*, vol. 48, no. 12, pp. 2429–2442, Jun. 2005.

[32] S. Moghaddam, "Microscale study of nucleation process in boiling of low-surface-tension liquids," Ph.D. dissertation, Univ. Maryland, College Park, MD, 2006.

[33] [Online]. Available: http://www.dow.com/cyclotene/index.htm

[34] Y. Y. Hsu, "On the size range of active nucleation cavities on a heating surface," *J. Heat Transfer*, vol. 84, pp. 207–215, 1962.

[35] S. Moghaddam, M. Ohadi, and J. Qi, "Pool boiling of water and FC-72 on copper and graphite foams," in *Proc. ASME InterPACK'3, Int. Electron. Packag. Tech. Conf. Exhib.*, Maui, HI, Jul. 6–11, 2003. Interpack2003-35316.

[36] A. Singh, B. B. Mikic, and W. M. Rohsenow, "Effect of superheat and cavity size on frequency of bubble departure in boiling," *J. Heat Transfer*, vol. 99, pp. 401–406, 1976.

[37] L. Brunetti and E. Monticone, "Properties of nickel thin films on polyimide substrate for HF bolometers," *Meas. Sci. Technol.*, vol. 4, pp. 1244–1248, 1993.
[38] Omega Engineering, Inc., *Omega Temperature Handbook*, 2000, Philadelphia, PA: Curtis Publishing Company.
[39] L. Ott, *Introduction to Statistical Methods and Data Analysis*. Pacific Grove, CA: Duxbury Press, 1977.
[40] S. Pinel, A. Marty, J. Tasselli, J. P. Bailbe, E. Beyne, R. Van Hoof, S. Marco, J. R. Morante, O. Vendier, and M. Huan, "Thermal modeling and management in ultrathin chip stack technology," *IEEE Trans. Compon. Packag. Technol.*, vol. 25, no. 2, pp. 244–253, Jun. 2002.

Saeed Moghaddam received the B.S. and M.S. degrees in mechanical engineering from Sharif University of Technology, Tehran, Iran, in 1993 and 1995, respectively, and the Ph.D. degree in mechanical engineering from the University of Maryland (UMD), College Park, in 2006.

He is the Vice President of Research and Development in Advanced Environmental Energy Concepts Inc., College Park and a Research Affiliate with the Department of Mechanical Engineering, UMD. He has published more than 15 technical papers. He is the holder of four patents. His current research interests include the area of micro/nanoscale heat and mass transport, micro/nanofluidics, smart thermal systems, and electronic cooling.

Dr. Moghaddam is a member of the American Society of Mechanical Engineers, American Society of Heating, Refrigerating, and Air Conditioning Engineers, and Society for Experimental Mechanics. He is an Associate Member of Sigma Xi, UM Chapter. He received the Best M.S. Thesis of the Year Award from the Iranian Society of Mechanical Engineers in 1996.

Kenneth T. Kiger received the B.S.A.E. and M.S.A.E. degrees from the University of Southern California, Los Angeles, in 1991 and 1993, respectively, and the Ph.D. degree in applied mechanics from the University of California, San Diego, in 1995.

In 1995, he joined the faculty of the Department of Mechanical Engineering, University of Maryland, College Park, where he is currently an Associate Professor. He has published more than 40 technical papers. His research interests include a broad range of fluid mechanics, heat transfer, and experimental techniques, specifically in the topics of multiphase flows, microscale study of dynamics of spray cooling for electronic applications, particle/turbulence interaction, turbulent mixing in complex geometries, and development of two-phase particle image velocimetry methods.

Dr. Kiger is a Reviewer of the National Science Foundation and a Referee for the Journal of Fluid Mechanics, Physics of Fluids, American Society of Mechanical Engineers Journal of Fluids Engineering, Experiments in Fluids, International Journal of Multiphase Flow, and Experimental Thermal and Fluid Sciences. He received the National Science Foundation CAREER Initiation Award in 1997. He is a member of the American Physical Society's Division of Fluid Dynamics, American Society of Mechanical Engineers, and American Institute of Aeronautics and Astronautics.

Alireza Modafe received the B.S. degree in electrical engineering from Sharif University of Technology, Tehran, Iran, in 1993 and the M.S. degree in electrical engineering from Iran University of Science and Technology, Tehran, in 1997. He is currently working toward the Ph.D. degree at the University of Maryland, College Park. His M.S. thesis was focused on the development of a test system for deep-level transient spectroscopy of charge carrier traps in semiconductors.

In August 2000, he joined the MEMS Sensors and Actuators Laboratory, Department of Electrical and Computer Engineering, University of Maryland. His current research interests include development of power microelectromechanical devices such as electric micromotors and microgenerators using silicon, microball bearing technology, and spin-on low-k dielectric polymers.

Mr. Modafe is the recipient of the 2002 Spring MEMS Alliance Workshop Best Poster Award and the 2002 American Vacuum Society's (AVS) Graduate Research Award. He is a member of the Materials Research Society and AVS. He is an Associate Member of Sigma Xi: The Scientific Research Society.

Reza Ghodssi (S'92–M'96) received the B.S., M.S., and Ph.D. degrees in electrical engineering from the University of Wisconsin, Madison, in 1990, 1992, and 1996, respectively.

From 1997 to 1999, he was a Postdoctoral Associate and a Research Scientist with the Microsystems Technology Laboratories and the Gas Turbine Laboratory, Massachusetts Institute of Technology, Cambridge. He is an Associate Professor and the Director of the MEMS Sensors and Actuators Laboratory, Department of Electrical and Computer Engineering and the Institute for Systems Research, University of Maryland (UMD), College Park. He is also affiliated with the Fischell Department of Bioengineering, the Maryland NanoCenter, the University of Maryland Energy Research Center, and the Department of Materials Science and Engineering, UMD. He has more than 55 scholarly publications. His research interests include the design and development of microfabrication technologies and their applications to micro/nanosensors and actuators, and integrative microsystems for chem-bio sensing and small-scale energy conversion.

Dr. Ghodssi was recently selected as an Editor for the "Handbook of MEMS Materials and Processes" that will be published in 2009. He is the recipient of the 2001 UMD George Corcoran Award, the 2002 National Science Foundation CAREER Award, and the 2003 UMD Outstanding Systems Engineering Faculty Award. He is among the 83 nation's outstanding engineers invited to attend the National Academy of Engineering's 2007 U.S. Frontiers of Engineering Symposium. He is the cofounder of MEMS Alliance in the greater Washington area. He is a member of the American Vacuum Society, Materials Research Society, American Society for Engineering Education, and American Association for the Advancement of Science.